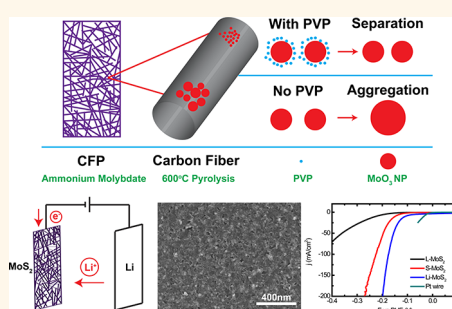# Electrochemical Tuning of MoS₂ Nanoparticles on Three-Dimensional Substrate for Efficient Hydrogen Evolution

Haotian Wang,[†,⊥] Zhiyi Lu,[‡,⊥] Desheng Kong,[‡] Jie Sun,[‡] Thomas M. Hymel,[‡] and Yi Cui[‡,§,*]

[†]Department of Applied Physics and [‡]Department of Materials Science and Engineering, Stanford University, 450 Serra Mall, Stanford, California 94305, United States and [§]Stanford Institute for Materials and Energy Sciences, SLAC National Accelerator Laboratory, 2575 Sand Hill Road, Menlo Park, California 94025, United States. [⊥]These authors contributed equally.

ABSTRACT Molybdenum disulfide (MoS₂) with the two-dimensional layered structure has been widely studied as an advanced catalyst for hydrogen evolution reaction (HER). Intercalating guest species into the van der Waals gaps of MoS₂ has been demonstrated as an effective approach to tune the electronic structure and consequently improve the HER catalytic activity. In this work, by constructing nanostructured MoS₂ particles with largely exposed edge sites on the three-dimensional substrate and subsequently conducting Li electrochemical intercalation and exfoliation processes, an ultrahigh HER performance with 200 mA/cm² cathodic current density at only 200 mV overpotential is achieved. We propose that both the high surface area nanostructure and the 2H semiconducting to 1T metallic phase transition of MoS₂ are responsible for the outstanding catalytic activity. Electrochemical stability test further confirms the long-term operation of the catalyst.

KEYWORDS: electrochemcial tuning · 2D material · MoS₂ nanoparticles · 3D substrate · hydrogen evolution reaction

The advent of graphene has intrigued intensive studies in layer-structured two-dimensional (2D) materials, including transition-metal dichalcogenides, due to their unique physical and chemical properties.[1] As a typical 2D material with rich physical and chemical properties and broad applications, molybdenum disulfide (MoS₂) has raised great attention recently. The strong Mo–S covalent bonding within the single molecular layers and the weak van der Waals interaction between them give rise to a strong anisotropy (Figure 1a). On the basis of this material property, a variety of MoS₂ morphologies, such as single layers,[2−5] single-wall nanotubes,[6] fullerene-like nanoparticles (NPs),[7] and layers of vertically aligned nanofilms,[8] were synthesized with different methods. In addition, the van der Waals gaps between the MoS₂ layers allow the guest species to be intercalated, thereby effectively tuning the MoS₂ electronic structures.[9−11] With these unique material properties and structures, MoS₂ has been used for transistors, lubricants, Li-ion batteries, and catalysis.[2,7,12−14]
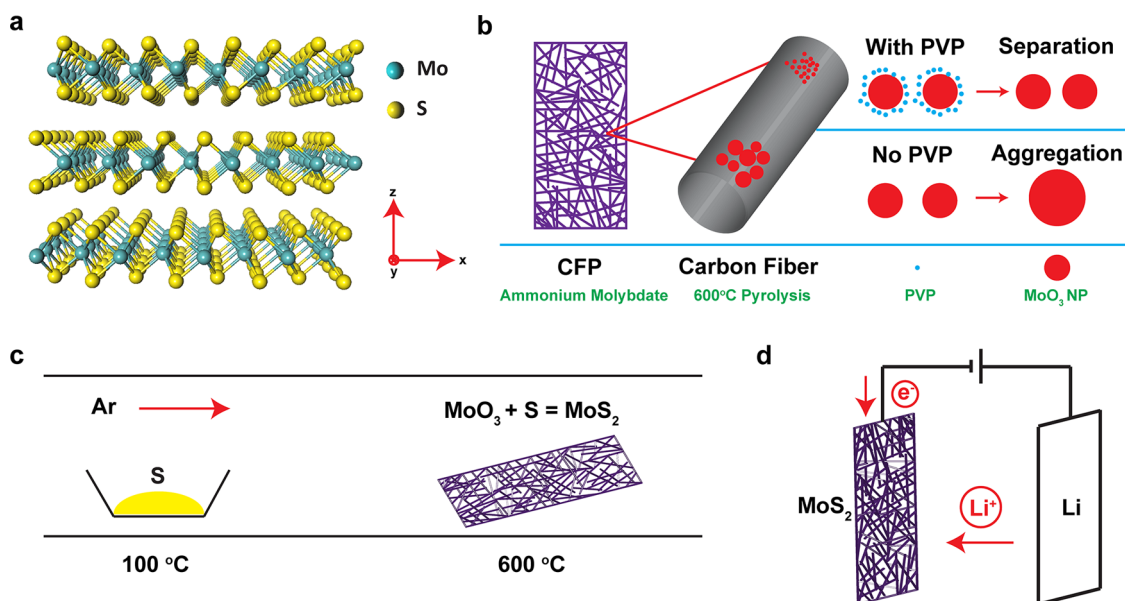
Among the broad range of applications of MoS₂, it has been extensively explored as a hydrogen evolution reaction (HER) catalyst recently.[15−17] Since the theoretical and experimental demonstrations identified the active edge sites of MoS₂ for HER,[15,16,18] scientists made efforts to largely expose the edge sites for enhanced activity by reducing the dimension of MoS₂ structures to the nanoscale.[17,19−21] In addition, the structures with rich HER active sites, such as amorphous films,[22,23] defective nanosheets,[24] and porous films,[25] showed high-performance HER activity per geometric area. MoS₂ on three-dimensional (3D) substrates with high surface area were also employed to improve the overall cathodic current.[26,27] Besides the morphology engineering of MoS₂, the electronic structure should be further optimized. Latest studies have demonstrated that chemically exfoliated 1T phase MoS₂ and WS₂ single-layer nanosheets are much more active in HER than their 2H phase counterparts,[28,29] and the electrochemical tuning of MoS₂

Figure 1. Schematic of material structure and synthesis. (a) Layered crystal structure of MoS₂.

Figure 1. Schematic of material structure and synthesis. (a) Layered crystal structure of MoS_2. (b) Schematic of the synthesis of large and small MoO_3 NPs on CFP. The CFP was first dipped into the ammonium molybdate solution with or without PVP additive. During the pyrolysis at 600 °C, the surface of the nucleated NPs may be coated by PVP molecules, which prevent those particles from further aggregation. Without the addition of PVP, the small particles tend to aggregate during the process and form large particles in the end. (c) Schematic of the rapid sulfurization setup in a horizontal tube furnace. (d) Schematic of the pouch battery cell configuration for Li electrochemical intercalation into MoS_2.

electronic structures showed both the strong electronic structure–catalytic activity correlation and the ability to optimize the HER activity.[11] Therefore, it is interesting and promising to apply electrochemical tuning and exfoliation to the high surface area, nanostructured MoS_2 on a 3D substrate for a highly active HER catalyst.

In our previous studies, we developed a flexible and rapid sulfurization/selenization process to convert Mo or MoO_3 thin films into edge-terminated $MoS_2/MoSe_2$ nanofilms.[8,11,30] Mo and MoO_3 thin films were obtained by DC magnetron sputtering and atomic layer deposition, respectively, which might limit the potential applications due to the involved high-vacuum systems and toxic precursors. In addition, the thin film morphology of Mo and MoO_3 was maintained after being converted to MoS_2, which did not increase the surface area by much. A facile, scalable, nontoxic, and low-cost method to synthesize Mo or MoO_3 nanosized structures over a three-dimensional large-area conducting surface is needed.

Here, we report a facile pyrolysis synthesis of MoO_3 NPs with sizes ∼30 nm on commercialized carbon fiber paper (CFP). MoS_2 NPs with exposed edge sites were then obtained by the rapid sulfurization process. The HER activity of as-grown 2H MoS_2 catalyst was largely improved by Li electrochemical tuning with layer exfoliation and 1T phase formation. The enhanced catalyst obtained 200 mA/cm² cathodic current at only 200 mV overpotential. Both long time cycling and continuous operation at constant voltage were performed to demonstrate the long-term stability of the catalyst.

RESULTS AND DISCUSSION

MoO_3 NPs were synthesized on a CFP substrate, as illustrated schematically in Figure 1b. CFP consists of conductive carbon fibers with ∼10 μm in diameter and several millimeters in length.[30] The carbon microfibers connect and fuse together to form a 3D conducting matrix, with ∼13 time surface area per geometric area (see Methods).[11] The 3D substrate can load more catalysts than the flat ones, thus helping to improve the catalytic performance per geometric area.[26] CFP was first treated by O_2 plasma to make it hydrophilic and then dipped into the 25 wt % ammonium heptamolybdate ((NH_4)$_6$$Mo_7$$O_{24}$·$4H_2O$) solution and dried on a hot plate with the salt uniformly distributed on the substrate (see Methods). The substrate was then heated up to 600 °C under Ar atmosphere in a tube furnace, where the ammonium heptamolybdate decomposed to produce MoO_3 (see Methods).[31] The sizes of the as-grown MoO_3 particles are around several hundred nanometers (we denote these as L-MoO_3) as shown in the scanning electron microscopy (SEM) image and the particle size distribution in Figure 2a and Supporting Information Figure S1a. The selected areas in the red boxes in Figure 2 are used for the statistical analysis of the particle size distributions, which is summarized in Figure S1. To shrink the size of the MoO_3 particle, 4 wt % polyvinylpyrrolidone (PVP) was added into the solution. Accordingly, uniformly distributed MoO_3 nanoparticles with ∼30 nm in diameters (we denote these as S-MoO_3) on carbon fibers were synthesized (Figures 2b and S1b). It is proposed in Figure 1b that PVP can help to disperse the salt on the
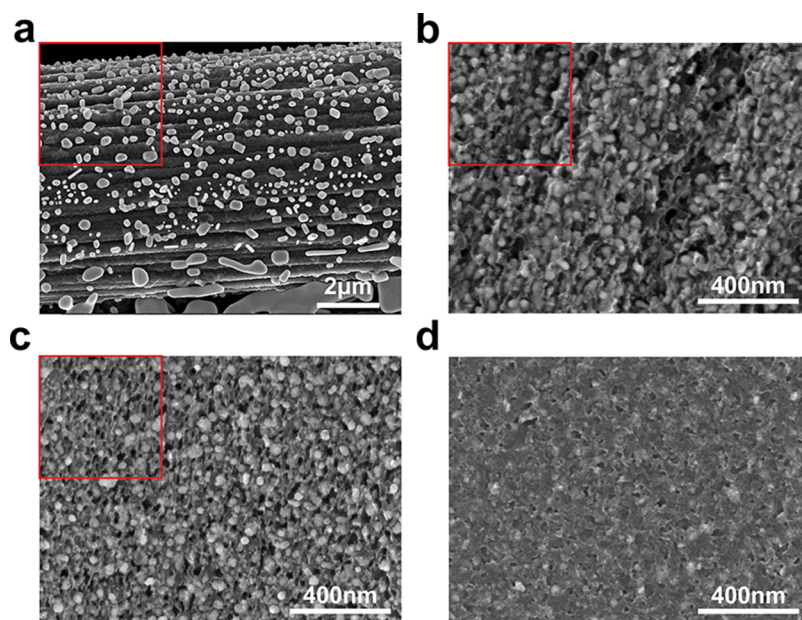
Figure 2. SEM images of the as-grown materials. (a) SEM image of L-MoO$_3$ NPs on CFP. (b) SEM image of S-MoO$_3$ NPs on CFP. The size of the NPs is obviously reduced from L-MoO$_3$. (c) SEM image of S-MoS$_2$ NPs on CFP. The morphology of S-MoS$_2$ is not changed from S-MoO$_3$ after the rapid sulfurization process. (d) SEM image of Li-MoS$_2$ on CFP. The structure of S-MoS$_2$ is totally destroyed after the lithiation and exfoliation processes. The red boxes in (a−c) represent the selected areas for the statistical analysis of the particle size distributions.

carbon fibers and was coated on the surface of the nucleated NPs during the pyrolysis process to prevent them from further aggregation.

The as-grown S-MoO$_3$ NPs were then put into a tube furnace for rapid sulfurization and converted into S-MoS$_2$ NPs, as illustrated in Figure 1c (see Methods).[8,30] The sulfur source we use is elemental sulfur instead of hydrogen sulfide.[19] The morphologies of the NPs are not significantly changed, as shown in Figures 2c and S1c. To conduct lithium (Li) electrochemical intercalation, we used the as-synthesized S-MoS$_2$ NPs as the cathode and two pieces of Li metal as the anodes to construct a pouch battery cell (see Methods). The galvanostatic discharge curve in Figure S2 offers rich information about the MoS$_2$ 2H to 1T phase transition as a well-defined discharge plateau is observed. The 2H phase is semiconducting, whereas the 1T is metallic.[10] The phase transition capacity also gives us a rough idea about the mass loading of MoS$_2$ on CFP (Supporting Information). The electrochemical tuning voltage was chosen to be 0.7 V vs Li$^+$/Li, where the 2H to 1T transition is complete but conversion reaction is not initiated yet.[32] After the Li intercalation, the electrode was washed by ethanol in which the intercalated Li in MoS$_2$ reacted with ethanol and partially exfoliated MoS$_2$.[11] The lithiation-treated S-MoS$_2$ is denoted as Li-MoS$_2$. The SEM image in Figure 2d shows that the S-MoS$_2$ NP structure was completely destroyed by the lithiation and exfoliation processes.[28]

X-ray photoelectron spectroscopy (XPS) was employed to characterize the samples at each synthesis stage in Figure 3a. All of the spectra were calibrated by C 1s peak located at 284.50 eV.[11] The Mo 3d$_{5/2}$ and 3d$_{3/2}$

peaks of S-MoO$_3$ were located at 232.4 and 235.4 eV, respectively, indicating a +6 oxidation state of Mo.[33] The binding energies of Mo shifted toward lower positions at 229.3 and 232.4 eV, respectively, after the sulfurization process, which suggests the formation of MoS$_2$.[11,19] The S 2p$_{1/2}$ and 2p$_{3/2}$ peaks are also shown in Figure S3. The electronic structure change, which is the MoS$_2$ 2H to 1T phase transition, following the Li intercalation and exfoliation processes, is reflected in the change of the Mo 3d region.[11] The formation of 1T MoS$_2$ shifts and broadens the Mo 3d peaks, suggesting that the new peaks emerge at lower binding energies. To extract more information about the phase transition process from the XPS spectrum, we fit the Mo 3d region by a rigorous procedure (fix the binding energy difference between the Mo 3d$_{3/2}$ and the Mo 3d$_{5/2}$ states at ∼3.10 eV).[34] The 2H and 1T MoS$_2$ peaks were obtained after the deconvolution of the Mo 3d peaks in Figure 3a, with a separation of binding energy at ∼0.9 eV.[11,29,35,36] The peak positions of 2H and 1T Mo 3d$_{5/2}$ are 229.3 and 228.4 eV, respectively. The ratio of MoS$_2$ 2H to 1T phase is estimated to be 0.82 by integrated intensities of the Mo 3d$_{5/2}$ peak.[11] Additional Mo 3d$_{5/2}$ and 3d$_{3/2}$ peaks were observed at 232.5 and 235.5 eV, respectively, indicating the surface oxidation during the sample preparation.

The compositions and phases of the as-grown samples were further confirmed by Raman spectroscopy in Figure 3b. The distinguished peaks in the S-MoO$_3$ Raman spectrum agree well with previous studies.[37,38] The S-MoS$_2$ Raman spectrum provides insight into the MoS$_2$ layer orientations. As shown in the inset, the peaks at 379 and 403 cm^{-1} represent the E$_{2g}^1$ and A$_{1g}$ modes,
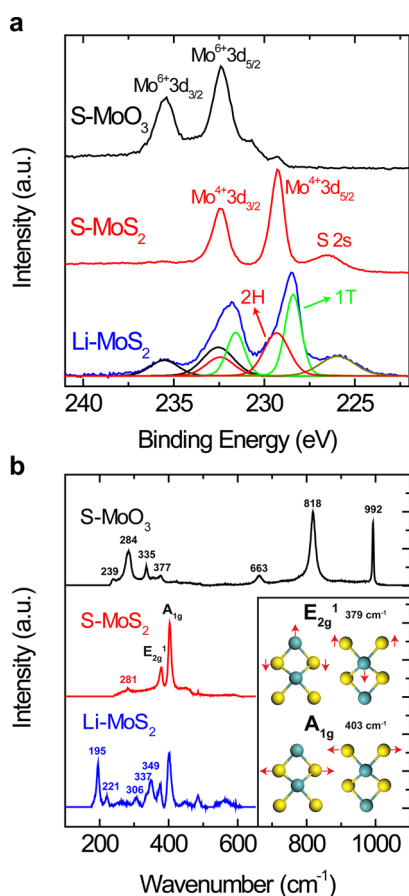
Figure 3. Characterizations of as-synthesized materials. (a) XPS spectra of S-MoO$_3$, S-MoS$_2$, and Li-MoS$_2$ samples. The broad Mo regions in the Li-MoS$_2$ spectrum are deconvoluted into red and green peaks, corresponding to 2H MoS$_2$ and 1T MoS$_2$, respectively. The black peaks in Li-MoS$_2$ represent the Mo^{6+} species, possibly from the surface oxidation during the sample preparation. **(b)** Raman spectra of S-MoO$_3$, S-MoS$_2$, and Li-MoS$_2$ samples. New peaks located at 195, 221, 306, 337, and 349 cm^{-1} are observed in Li-MoS$_2$ compared with S-MoS$_2$, confirming the 1T phase MoS$_2$ formation. The inset represents the atomic vibration direction of E$_{2g}^1$ and A$_{1g}$ Raman modes of MoS$_2$.

respectively. The peak intensity corresponding to different vibration modes depends on the layer orientations.[8,30] The A$_{1g}$ mode is preferentially excited in the spectrum as compared with the E$_{2g}^1$ mode, indicating the NPs are terminated by edges on the surface.[8,11] The presence of 1T phase MoS$_2$ in Li-MoS$_2$ is confirmed by the additional Raman peaks emerging at 195, 221, 306, 337, and 349 cm^{-1}, respectively.[11,28,35,39] The integrated intensity ratio of E$_{2g}^1$ to A$_{1g}$ is obviously increased from S-MoS$_2$, which suggests that the Li intercalation and exfoliation processes change the morphology and orientation of the MoS$_2$ NPs.[28] Additional bulk information of the as-synthesized samples was detected by X-ray diffraction (XRD) and is summarized in Figure S4.

The catalytic activities of L-MoS$_2$, S-MoS$_2$, and Li-MoS$_2$ samples were examined in a standard three-electrode electrochemical cell setup with 0.5 M H$_2$SO$_4$ solution (see Methods). Cyclic voltammograms (CVs) were taken

several cycles to bubble away the surface contaminates and at the same time stabilize the catalysts. Electrochemical impedance spectroscopy performed at −0.12 V *versus* reversible hydrogen electrode (RHE) in Figure S5 shows very small series resistances of the as-grown catalysts and the testing system. The polarization curves and Tafel plots after *iR* correction in Figure 4a,b were obtained at a voltage sweeping rate of 5 mV/s. The L-MoS$_2$ NPs give out the lowest HER catalytic activity, with a Tafel slope of 101 mV/decade and an exchange current density of 0.063 mA/cm^2. The HER activity was largely improved in terms of both Tafel slope and onset potential when the size of the particles was shrunken. S-MoS$_2$ exhibits a lower Tafel slope of 66 mV/decade, with roughly the same exchange current density of 0.050 mA/cm^2. The small dimension of the NPs has several positive effects on the HER catalytic activity. First of all, the smaller NP guarantees better electrical conductivity from the substrate to the surface sites. Second, the smaller NP bonds with the substrate on a relatively larger surface area fraction, which may result in a stronger bonding with the substrate than that of the larger NP and favors the long-term cycling stability of the catalyst. Third, the small NP results in a large surface curvature which may help to expose more HER active sites and enhance the activity of the catalytic center.[30]

The 1T MoS$_2$ has been demonstrated to be more active than 2H MoS$_2$ due to the much higher conductivity and additional catalytically active sites on the terrace.[29,36] The HER activity of S-MoS$_2$ NPs was further boosted by Li electrochemical tuning of the MoS$_2$ electronic structure.[11,28] As shown in Figure 4a, the Li-MoS$_2$ reaches 200 mA/cm^2 cathodic current density at only 200 mV overpotential, where the L-MoS$_2$ and S-MoS$_2$ catalysts only arrive at 6 and 57 mA/cm^2, respectively. This result is also better than some recently published works listed in Table S1. The largely enhanced catalytic activity is mainly due to the improved exchange current density of 0.167 mA/cm^2, more than 3 times that of S-MoS$_2$. Li-MoS$_2$ exhibits a 62 mV/decade Tafel slope comparable to S-MoS$_2$. The resulting Tafel slope is different from the 1T MoS$_2$ nanofilm on CFP (44 mV/decade) in our previous study, likely due to the different morphologies.[8,30] It should be noted that in Figure 4b the Tafel plots of L-MoS$_2$, S-MoS$_2$, and Pt wire bend at large cathodic current regions due to severe bubble adhesion on the surface of the electrode, which will block the contact between the catalyst and the electrolyte and decrease the HER efficiency.[40] In Figure 4a, the polarization curve of S-MoS$_2$ oscillates when reaching high cathodic current, again indicating that the bubble releasing at high current may affect the HER catalytic activity. However, Li-MoS$_2$ shows a smooth polarization curve in Figure 4a and a long linear region without observable bending in Figure 4b, indicating a possible facilitated bubble releasing process compared to both L-MoS$_2$ and S-MoS$_2$. This advantage
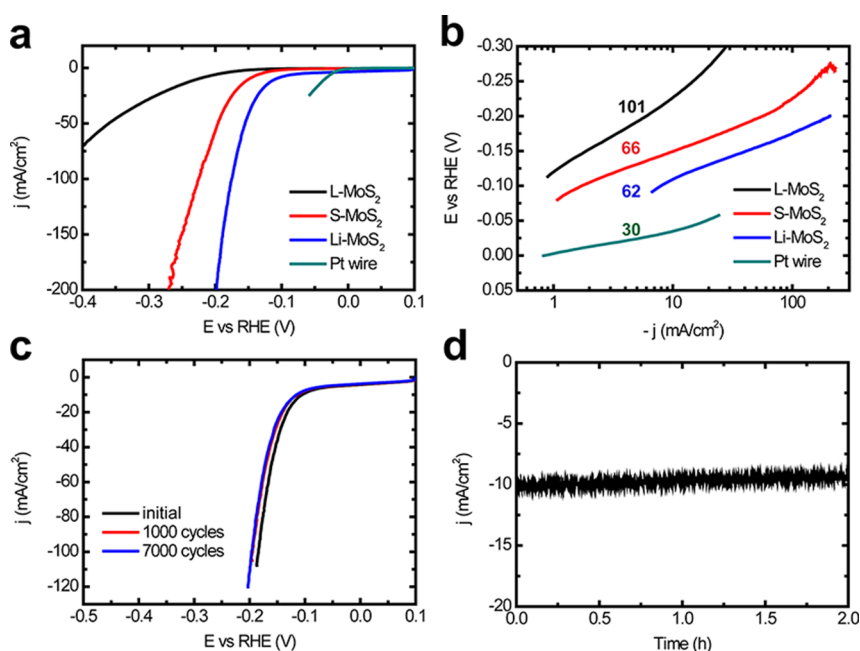
Figure 4. Electrochemical characterizations of as-grown catalysts on CFP. (a) Polarization curves of L-MoS$_2$, S-MoS$_2$, Li-MoS$_2$, and Pt wire at a scan rate of 5 mV/s. S-MoS$_2$ shows a much higher HER activity than does L-MoS$_2$, due to the reduced size of NPs. The performance of Li-MoS$_2$ is further enhanced after the Li electrochemical tuning and exfoliation processes, achieving 200 mA/cm^2 cathodic current at only −200 mV overpotential. (b) Tafel plots of L-MoS$_2$, S-MoS$_2$, Li-MoS$_2$, and Pt wire. Li-MoS$_2$ shows the largest linear region. (c) Polarization curves of Li-MoS$_2$ catalyst at a scan rate of 5 mV/s after CV cycles for stability test. The CVs were taken at a scan rate of 100 mV/s between −0.35 and 0.1 V *vs* RHE before *iR* correction to reach a high cathodic current of ∼100 mA/cm^2 for 7000 cycles. The HER activity of Li-MoS$_2$ shows a negligible decay after the first 1000 cycles but remains unchanged until 7000 cycles. (d) Potentiostatic electrolysis of Li-MoS$_2$ for 2 h. The potential we applied is −118 mV *vs* RHE after *iR* correction. The cathodic current remains stable during the operation, indicating that the catalyst is stable under HER conditions.

helps Li-MoS$_2$ to enlarge the performance enhancement over the other two catalysts at high current regions.

In addition, to dig out more information about the 1T-MoS$_2$ catalytic activity, we synthesized lithiation-treated MoS$_2$ with different 2H to 1T MoS$_2$ ratio and compared it with the HER activity of Li-MoS$_2$. The lithiation voltage was set at 1.1 V *vs* Li$^+$/Li (higher than the 0.7 V lithiation voltage of Li-MoS$_2$), thus we denote the sample as 1.1-V MoS$_2$. On the basis of the XPS spectrum shown in Figure S6, we successfully obtained the 2H to 1T phase ratio of 2.67 in 1.1-V MoS$_2$, with less percentage of 1T phase than Li-MoS$_2$ (2H to 1T ratio is 0.82). The HER performance of 1.1-V MoS$_2$ is improved from S-MoS$_2$ but inferior to Li-MoS$_2$ in Figure S7, demonstrating that the 1T phase of MoS$_2$ is more active than its 2H counterpart.

Stability has always been an essential aspect in catalyst evaluation since material durability has to be considered for long-term utilization. The stability study on the most active Li-MoS$_2$ catalyst was carried out by taking continuous CV cycles and potentiostatic electrolysis. In Figure 4c, the CVs were taken at a scan rate of 100 mV/s between −0.35 and 0.1 V *vs* RHE before *iR* correction to reach a high cathodic current of ∼100 mA/cm^2 for 7000 cycles. The polarization curves were obtained after 1000 cycles at 5 mV/s with *iR* correction. The HER activity shows a negligible decay after the first 1000 cycles but remains unchanged until 7000 cycles. In addition, when operating HER at a constant

overpotential of −118 mV *vs* RHE after *iR* correction, a stable corresponding current density of ∼10 mA·cm^{-2} was observed on this Li-MoS$_2$ electrode with negligible degradations after 2 h testing, revealing its excellent stability under HER conditions. Li-MoS$_2$ exhibits excellent electrochemical stability even after the Li intercalation and exfoliation processes, suggesting that the MoS$_2$ NPs bind strongly on the CFP substrate through the high-temperature sulfurization.[30]

The HER catalytic activities of L-MoS$_2$, S-MoS$_2$, and Li-MoS$_2$ are associated with their different morphologies and electronic properties. The size of the synthesized MoS$_2$ NPs may result in different effective surface areas, which play very important roles in the overall HER performance.[23,26,28] To estimate the effective surface areas, we employed the CV method to measure the electrochemical double-layer capacitances (EDLCs), C_{dl}, as shown in Figure 5.[23,28,41] The potential range where no faradic current was observed was selected for the catalysts. Slow voltage scan rates were chosen for accurate measurements of the large surface area electrodes. The halves of the positive and negative current density differences at the center of the scanning potential ranges are plotted *versus* the voltage scan rates in Figure 5d, in which the slopes are the EDLCs. The electrochemical effective surface area is increased by 3 times when the MoS$_2$ particle size is reduced from around several hundred to tens of
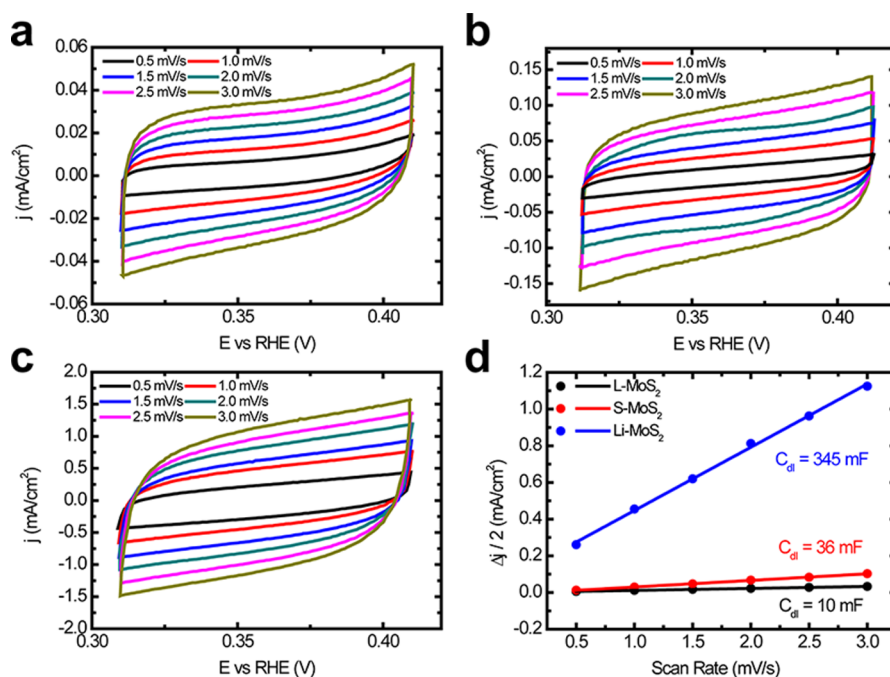
Figure 5. Electrochemical double-layer capacitance measurements. (a–c) Electrochemical cyclic voltammogram of as-grown catalysts at different potential scanning rates. The scan rates are 0.5, 1.0, 1.5, 2.0, 2.5, and 3.0 mV/s. The selected potential range where no faradic current was observed is 0.31 to 0.41 V *vs* RHE. **(d)** Linear fitting of the capacitive currents of the catalysts *vs* scan rates. The calculated double-layer capacitances are 10, 36, and 345 mF for L-MoS$_2$, S-MoS$_2$, and Li-MoS$_2$, respectively.

nanometers. This result is consistent with our rough estimation, as illustrated in Supporting Information. The EDLC is further improved by nearly 10 times when S-MoS$_2$ NPs are lithiated and exfoliated to Li-MoS$_2$. The lithiation and exfoliation processes open up the van der Waals gaps of MoS$_2$ and expose more effective sites on the terrace surface. The Li intercalation process induces phase transition into 1T MoS$_2$, in which the strained terrace sites have been shown to be active for HER.[29,36] The Li electrochemical tuning of MoS$_2$ electronic structures not only helps to enhance the conductivity of the catalyst but also creates HER active sites on the terrace surface other than the edge sites, which boosts the overall HER activity of the catalyst. In addition, the relationship between the enhanced conductivities and the corresponding Tafel slopes of the catalysts can be revealed by electrochemical impedance spectroscopy,[42] which is of interest and importance for future studies.

To further understand the intrinsic catalytic property of the as-synthesized Li-MoS$_2$ catalyst, we studied the turnover frequency (TOF) of the catalyst which describes the average activity of each HER active site.[8,16] On the basis of our previous study of MoS$_2$ nanofilm on flat glassy carbon,[8] it is straightforward to obtain the TOF of Li-MoS$_2$ assuming that the EDLC scales with the density of the effective sites.[23] The EDLC of MoS$_2$ nanofilm shown in Figure S8 is 29 μF/cm^2, consistent with the previous studies of flat electrodes.[23,43,44] Detailed calculations under Figure S8 illustrates that the TOF of Li-MoS$_2$ is ~0.1 H$_2$/s per site at 200 mV overpotential (200 mA/cm^2), comparable with previous studies.[22,23]

CONCLUSION

In conclusion, we have successfully synthesized nanostructured MoS$_2$ particles with preferentially exposed edge sites on the 3D CFP substrate by the facile pyrolysis and sulfurization methods. By Li electrochemical intercalation and layer exfoliation, we are able to tune the electronic structures of MoS$_2$ from 2H to 1T phase, exposing more HER active sites and thus boosting the catalytic activity. High HER activity and electrochemical stability of Li-MoS$_2$ catalyst have been demonstrated. This work provides a cost-effective and efficacious protocol to fabricate 3D materials with tunable electronic properties, which is not only appropriate in electrochemical catalysis but also applicable for other electronic devices.

METHODS

Material Synthesis and Preparation. CFP (from Fuel Cell Store, 2050-A) used in our study is ~200 μm thick. To quantify the specific area, CFP is activated by oxygen plasma and then conformally coated with a 50 nm thick Al$_2$O$_3$ layer by atomic layer deposition (Cambridge NanoTech Savannah 100 atomic layer deposition system). The coating is about 0.26 mg/cm^2 determined by using a microbalance (Sartarious SE2, 0.1 μg resolution). It suggests that the roughness factor of the carbon fiber paper is ~13.

CFP was first activated by O_2 plasma for 5 min before being dipped into the solution. The surface of the CFP is hydrophobic, which prevents the substrate from being completely wetted by the solution. The O_2 plasma helps to create hydrophilic functional groups on the surface of the carbon fiber, which helps the substrate absorb the solution and form a uniform solution layer on the 3D surface. CFP dipped with ammonium heptamolybdate (Fisher Scientific) and polyvinylpyrrolidone (Sigma-Aldrich, wt 360 000) was then put into a single-zone, 12 in. horizontal tube furnace (Lindberg/Blue M) equipped with a 1 in. diameter quartz tube. The CFP coated with the salt was placed at the hot center of the tube furnace. The pressure and flow rate of the Ar gas were kept at 1000 mTorr and 100 sccm, respectively, during the thermal decomposition process. The heating center of the furnace was increased to a reaction temperature of 600 °C in 30 min, and then held at that reaction temperature for 90 min, followed by natural cool down.

The as-grown MoO_3 on CFP was then put into another quartz tube for rapid sulfurization process. Sulfur powder (99.99%, from Sigma Aldrich) was placed on the upstream side of the furnace at carefully adjusted locations to set the temperature. Ar gas was used as the precursor carrier, and the pressure and flow rate were kept at 1000 mTorr and 100 sccm, respectively, during the growth. The heating center of the furnace was increased to a reaction temperature of 600 °C in 20 min, and the sulfur precursor was kept at around 200 °C. The furnace was held at that reaction temperature for 10 min, followed by natural cool down. The mass loading of the as-grown MoS_2 on CFP is about 3.4 to 3.9 mg/cm^2 determined by the microbalance.

The as-grown MoS_2 on CFP was then made into a battery configuration acting as the cathode, combined with Li metal on each side of CFP as the anode and 1.0 M $LiPF_6$ in 1:1 w/w ethylene carbonate/diethyl carbonate (EMD Chemicals) as the electrolyte. The galvanostatic discharge currents for MoS_2 samples were set at 125 μA/cm^2. After the discharge process, samples were cleaned by ethanol to remove the electrolyte on the surface.

Characterizations. Characterizations were carried out using scanning electron microscopy (SEM, FEI Nova NanoSEM 450), X-ray photoelectron spectroscopy (XPS, SSI SProbe XPS spectrometer with Al Kα source), Raman spectroscopy (531nm excitation laser, cutoff around 175 cm^{-1}, WITEC Raman spectrometer), and X-ray diffraction (PANalytical X'Pert diffractometer with Cu Kα radiation).

Electrochemical Studies. The as-grown catalysts on CFP were tested in 0.5 M H_2SO_4 solution (deaerated by N_2) using a typical three-electrode electrochemical cell setup, with a saturated calomel electrode (E(RHE) = E(SCE) + 0.280 V after calibration) as the reference electrode and a graphite rod (99.999%, from Sigma Aldrich) as the counter electrode. Electrochemically inert kapton tape was used to define the 1 cm^2 electrode area. Linear sweep voltammetry, CVs, and AC impedance spectroscopy are recorded by a Biologic VSP potentiostat.

Conflict of Interest: The authors declare no competing financial interest.

Supporting Information Available: Additional details on sample chracterizations, electrochemical measurements, and analyses. This material is available free of charge *via* the Internet at http://pubs.acs.org.

REFERENCES AND NOTES

1. Novoselov, K. S.; Geim, A. K.; Morozov, S. V.; Jiang, D.; Zhang, Y.; Dubonos, S. V.; Grigorieva, I. V.; Firsov, A. A. Electric Field Effect in Atomically Thin Carbon Films. *Science* **2004**, *306*, 666–669.

2. Yin, Z.; Li, H.; Li, H.; Jiang, L.; Shi, Y.; Sun, Y.; Lu, G.; Zhang, Q.; Chen, X.; Zhang, H. Single-Layer MoS_2 Phototransistors. *ACS Nano* **2012**, *6*, 74–80.

3. Splendiani, A.; Sun, L.; Zhang, Y.; Li, T.; Kim, J.; Chim, C.-Y.; Galli, G.; Wang, F. Emerging Photoluminescence in Monolayer MoS_2. *Nano Lett.* **2010**, *10*, 1271–1275.

4. Ji, Q.; Zhang, Y.; Gao, T.; Zhang, Y.; Ma, D.; Liu, M.; Chen, Y.; Qiao, X.; Tan, P.-H.; Kan, M.; *et al.* Epitaxial Monolayer MoS_2 on Mica with Novel Photoluminescence. *Nano Lett.* **2013**, *13*, 3870–3877.

5. Najmaei, S.; Liu, Z.; Zhou, W.; Zou, X.; Shi, G.; Lei, S.; Yakobson, B. I.; Idrobo, J.-C.; Ajayan, P. M.; Lou, J. Vapour Phase Growth and Grain Boundary Structure of Molybdenum Disulphide Atomic Layers. *Nat. Mater.* **2013**, *12*, 754–759.

6. Remskar, M.; Mrzel, A.; Skraba, Z.; Jesih, A.; Ceh, M.; Demšar, J.; Stadelmann, P.; Lévy, F.; Mihailovic, D. Self-Assembly of Subnanometer-Diameter Single-Wall MoS_2 Nanotubes. *Science* **2001**, *292*, 479–481.

7. Chhowalla, M.; Amaratunga, G. A. J. Thin Films of Fullerene-like MoS_2 Nanoparticles with Ultra-low Friction and Wear. *Nature* **2000**, *407*, 164–167.

8. Kong, D.; Wang, H.; Cha, J. J.; Pasta, M.; Koski, K. J.; Yao, J.; Cui, Y. Synthesis of MoS_2 and $MoSe_2$ Films with Vertically Aligned Layers. *Nano Lett.* **2013**, *13*, 1341–1347.

9. Divigalpitiya, W. M. R.; Frindt, R. F.; Morrison, S. R. Inclusion Systems of Organic Molecules in Restacked Single-Layer Molybdenum Disulfide. *Science* **1989**, *246*, 369–371.

10. Py, M. A.; Haering, R. R. Structural Destabilization Induced by Lithium Intercalation in MoS_2 and Related Compounds. *Can. J. Phys.* **1983**, *61*, 76–84.

11. Wang, H.; Lu, Z.; Xu, S.; Kong, D.; Cha, J. J.; Zheng, G.; Hsu, P.-C.; Yan, K.; Bradshaw, D.; Prinz, F. B.; *et al.* Electrochemical Tuning of Vertically Aligned MoS_2 Nanofilms and Its Application in Improving Hydrogen Evolution Reaction. *Proc. Natl. Acad. Sci. U.S.A.* **2013**, *110*, 19701–19706.

12. Radisavljevic, B.; Radenovic, A.; Brivio, J.; Giacometti, V.; Kis, A. Single-Layer MoS_2 Transistors. *Nat. Nanotechnol.* **2011**, *6*, 147–150.

13. Chang, K.; Chen, W. *In Situ* Synthesis of MoS_2/Graphene Nanosheet Composites with Extraordinarily High Electrochemical Performance for Lithium Ion Batteries. *Chem. Commun.* **2011**, *47*, 4252–4254.

14. Byskov, L. S.; Nørskov, J. K.; Clausen, B. S.; Topsøe, H. DFT Calculations of Unpromoted and Promoted MoS_2-Based Hydrodesulfurization Catalysts. *J. Catal.* **1999**, *187*, 109–122.

15. Hinnemann, B.; Moses, P. G.; Bonde, J.; Jørgensen, K. P.; Nielsen, J. H.; Horch, S.; Chorkendorff, I.; Nørskov, J. K. Biomimetic Hydrogen Evolution: MoS_2 Nanoparticles as Catalyst for Hydrogen Evolution. *J. Am. Chem. Soc.* **2005**, *127*, 5308–5309.

16. Jaramillo, T. F.; Jørgensen, K. P.; Bonde, J.; Nielsen, J. H.; Horch, S.; Chorkendorff, I. Identification of Active Edge Sites for Electrochemical H_2 Evolution from MoS_2 Nanocatalysts. *Science* **2007**, *317*, 100–102.

17. Li, Y.; Wang, H.; Xie, L.; Liang, Y.; Hong, G.; Dai, H. MoS_2 Nanoparticles Grown on Graphene: An Advanced Catalyst for the Hydrogen Evolution Reaction. *J. Am. Chem. Soc.* **2011**, *133*, 7296–7299.

18. Tsai, C.; Abild-Pedersen, F.; Nørskov, J. K. Tuning the MoS_2 Edge-Site Activity for Hydrogen Evolution *via* Support Interactions. *Nano Lett.* **2014**, *14*, 1381–1387.

19. Chen, Z.; Cummins, D.; Reinecke, B. N.; Clark, E.; Sunkara, M. K.; Jaramillo, T. F. Core—Shell MoO_3—MoS_2 Nanowires for Hydrogen Evolution: A Functional Design for Electrocatalytic Materials. *Nano Lett.* **2011**, *11*, 4168–4175.

20. Vrubel, H.; Merki, D.; Hu, X. Hydrogen Evolution Catalyzed by MoS_3 and MoS_2 Particles. *Energy Environ. Sci.* **2012**, *5*, 6136–6144.

21. Morales-Guio, C. G.; Stern, L.-A.; Hu, X. Nanostructured Hydrotreating Catalysts for Electrochemical Hydrogen Evolution. *Chem. Soc. Rev.* **2014**, 10.1039/C3CS60468C.

22. Merki, D.; Fierro, S.; Vrubel, H.; Hu, X. Amorphous Molybdenum Sulfide Films as Catalysts for Electrochemical Hydrogen Production in Water. *Chem. Sci.* **2011**, *2*, 1262–1267.

23. Benck, J. D.; Chen, Z.; Kuritzky, L. Y.; Forman, A. J.; Jaramillo, T. F. Amorphous Molybdenum Sulfide Catalysts for Electrochemical Hydrogen Production: Insights into the Origin of Their Catalytic Activity. *ACS Catal.* **2012**, *2*, 1916–1923.

24. Xie, J.; Zhang, H.; Li, S.; Wang, R.; Sun, X.; Zhou, M.; Zhou, J.; Lou, X. W.; Xie, Y. Defect-Rich MoS$_2$ Ultrathin Nanosheets with Additional Active Edge Sites for Enhanced Electrocatalytic Hydrogen Evolution. *Adv. Mater.* **2013**, *25*, 5807–5813.

25. Lu, Z.; Zhang, H.; Zhu, W.; Yu, X.; Kuang, Y.; Chang, Z.; Lei, X.; Sun, X. *In Situ* Fabrication of Porous MoS$_2$ Thin-Films as High-Performance Catalysts for Electrochemical Hydrogen Evolution. *Chem. Commun.* **2013**, *49*, 7516–7518.

26. Kibsgaard, J.; Chen, Z.; Reinecke, B. N.; Jaramillo, T. F. Engineering the Surface Structure of MoS$_2$ To Preferentially Expose Active Edge Sites for Electrocatalysis. *Nat. Mater.* **2012**, *11*, 963–969.

27. Chang, Y.-H.; Wu, F.-Y.; Chen, T.-Y.; Hsu, C.-L.; Chen, C.-H.; Wiryo, F.; Wei, K.-H.; Chiang, C.-Y.; Li, L.-J. Three-Dimensional Molybdenum Sulfide Sponges for Electrocatalytic Water Splitting. *Small* **2013**, *10*, 895–900.

28. Lukowski, M. A.; Daniel, A. S.; Meng, F.; Forticaux, A.; Li, L.; Jin, S. Enhanced Hydrogen Evolution Catalysis from Chemically Exfoliated Metallic MoS$_2$ Nanosheets. *J. Am. Chem. Soc.* **2013**, *135*, 10274–10277.

29. Voiry, D.; Yamaguchi, H.; Li, J.; Silva, R.; Alves, D. C. B.; Fujita, T.; Chen, M.; Asefa, T.; Shenoy, V. B.; Eda, G.; *et al.* Enhanced Catalytic Activity in Strained Chemically Exfoliated WS$_2$ Nanosheets for Hydrogen Evolution. *Nat. Mater.* **2013**, *12*, 850–855.

30. Wang, H.; Kong, D.; Johanes, P.; Cha, J. J.; Zheng, G.; Yan, K.; Liu, N.; Cui, Y. MoSe$_2$ and WSe$_2$ Nanofilms with Vertically Aligned Molecular Layers on Curved and Rough Surfaces. *Nano Lett.* **2013**, *13*, 3426–3433.

31. Hanafi, Z. M.; Khilla, M. A.; Askar, M. H. The Thermal Decomposition of Ammonium Heptamolybdate. *Thermochim. Acta* **1981**, *45*, 221–232.

32. Xiao, J.; Choi, D.; Cosimbescu, L.; Koech, P.; Liu, J.; Lemmon, J. P. Exfoliated MoS$_2$ Nanocomposite as an Anode Material for Lithium Ion Batteries. *Chem. Mater.* **2010**, *22*, 4522–4524.

33. Choi, J. G.; Thompson, L. T. XPS Study of As-Prepared and Reduced Molybdenum Oxides. *Appl. Surf. Sci.* **1996**, *93*, 143–149.

34. Vrubel, H.; Hu, X. Growth and Activation of an Amorphous Molybdenum Sulfide Hydrogen Evolving Catalyst. *ACS Catal.* **2013**, *3*, 2002–2011.

35. Eda, G.; Yamaguchi, H.; Voiry, D.; Fujita, T.; Chen, M.; Chhowalla, M. Photoluminescence from Chemically Exfoliated MoS$_2$. *Nano Lett.* **2011**, *11*, 5111–5116.

36. Voiry, D.; Salehi, M.; Silva, R.; Fujita, T.; Chen, M.; Asefa, T.; Shenoy, V. B.; Eda, G.; Chhowalla, M. Conducting MoS$_2$ Nanosheets as Catalysts for Hydrogen Evolution Reaction. *Nano Lett.* **2013**, *13*, 6222–6227.

37. Desikan, A. N.; Huang, L.; Oyama, S. T. Oxygen Chemisorption and Laser Raman Spectroscopy of Unsupported and Silica-Supported Molybdenum Oxide. *J. Phys. Chem.* **1991**, *95*, 10050–10056.

38. Garimella, S.; Drozd, V.; Durygin, A. High-Pressure Raman Study on the Decomposition of Polycrystalline Molybdenum Hexacarbonyl. *J. Inorg. Organomet. Polym.* **2009**, *19*, 415–421.

39. Julien, C. M. Lithium Intercalated Compounds: Charge Transfer and Related Properties. *Mater. Sci. Eng., R* **2003**, *40*, 47–102.

40. Lu, Z.; Zhu, W.; Yu, X.; Zhang, H.; Li, Y.; Sun, X.; Wang, X.; Wang, H.; Wang, J.; Luo, J.; *et al.* Ultrahigh Hydrogen Evolution Performance of Under-Water "Superaerophobic" MoS$_2$ Nanostructured Electrodes. *Adv. Mater.* **2014**, DOI: 10.1002/adma.201304759.

41. Merki, D.; Vrubel, H.; Rovelli, L.; Fierro, S.; Hu, X. Fe, Co, and Ni Ions Promote the Catalytic Activity of Amorphous Molybdenum Sulfide Films for Hydrogen Evolution. *Chem. Sci.* **2012**, *3*, 2515–2525.

42. Vrubel, H.; Moehl, T.; Gratzel, M.; Hu, X. Revealing and Accelerating Slow Electron Transport in Amorphous Molybdenum Sulphide Particles for Hydrogen Evolution Reaction. *Chem. Commun.* **2013**, *49*, 8985–8987.

43. Kötz, R.; Carlen, M. Principles and Applications of Electrochemical Capacitors. *Electrochim. Acta* **2000**, *45*, 2483–2498.

44. Xia, J.; Chen, F.; Li, J.; Tao, N. Measurement of the Quantum Capacitance of Graphene. *Nat. Nanotechnol.* **2009**, *4*, 505–509.